

# Vibration Analysis of Single-Phase Claw-Pole BLDC Fan Drives with Different Claw Geometries

Nejat Saed<sup>1,2</sup>, *Student Member, IEEE*, Shahin Asgari<sup>1,2</sup>, *Student Member, IEEE*, Klaus Krischan<sup>2</sup>, and Annette Muetze<sup>1,2</sup>, *Fellow, IEEE*

<sup>1</sup>Christian Doppler Laboratory for Brushless Drives for Pump and Fan Applications, Graz, Austria

<sup>2</sup>Electric Drives and Power Electronic Systems Institute, Graz University of Technology, Graz, Austria

**Abstract**—Fractional horsepower single-phase brushless DC (BLDC) machines are commonly used in auxiliary drives in automotive applications. Although the noise and vibration levels of these small machines may be generally low, and much lower than those of the propulsion drive(s), they may have detrimental effects on the passengers' comfort, notably when mounted close to the passengers or when generating noise in adjacent structures. This study focuses on a low-cost single-phase BLDC machine with a claw-pole stator structure and compares its vibration performance across various claw geometries to determine the most effective approach to minimize vibration. In total, seven different claw shapes were designed and prototyped for this analysis. In addition to conventional rectangular-shaped claws, not only the two previously presented modifications of skewing and adding auxiliary slots are applied to the claw geometry, but trapezoidal claw shapes are also analyzed. Here, the influences of claw length as well as of the asymmetric air-gap profile on vibration performance are studied. The results indicate that the asymmetric trapezoidal claw shape exhibits the best vibration performance, among the investigated designs.

**Index Terms**—Claw geometry, claw-pole machines, single-phase BLDC machines, vibration.

## I. INTRODUCTION

**B**RUSHLESS direct current (BLDC) motors are commonly used in low power variable-speed applications such as automotive pumps and fans, due to their high torque density [1], [2]. In automotive auxiliary applications, where cost is typically the primary design criterion for mass-produced fractional horsepower drives, single-phase BLDC machines are usually preferred over their three-phase counterparts. However, their high cogging torques and torque ripples can lead to noise and vibration.

Claw-pole single-phase BLDC machines have been proposed as a low-cost alternative for conventional salient-pole single-phase BLDC drives in fan applications [3], [4]. In fractional horsepower applications, claw-pole machines have thinner stator thickness than conventional machines to prevent high eddy current losses. This, however, results in a less stiff mechanical structure and thus possibly higher noise and vibration compared to their salient-pole stator counterparts [5].

The investigation of noise and vibration characteristics of fractional horsepower BLDC machines with claw-pole stators has remained relatively unexplored in the literature. Techniques proposed to mitigate noise and vibration of claw-pole

machines by modifying the claw geometry mainly have been applied to machines with higher power ratings and thicker claws, e.g., [6]–[8]. The implementation of these methods can be challenging for small machines due to the thin claws and small sizes. Skewing the claws and incorporating auxiliary slots have been identified as cost-effective solutions, as they do not introduce significant additional manufacturing cost in claw-pole stator manufacturing [4]. This is in contrast to salient-pole stators where a more intricate manufacturing process would be required, thus increasing production costs [9], [10].

This paper extensively expands upon the initial findings previously introduced in [1]. It extends the investigation into more geometry parameters of the claws including, claw length and asymmetric claw shape design. Furthermore, the vibration measurements have been expanded beyond single operation points to include the complete range of switching angles.

## II. OUTLINE AND METHODOLOGY

This study investigates the performances of a total of seven different claw geometries used in single-phase claw-pole BLDC motors, originally designed for a low-cost fan drive for auxiliary automotive applications. The primary objective of this study is to investigate the vibration characteristics of various claw designs, while also analyzing their electromagnetic and structural properties, as these factors initially generate the vibration and serve as the medium for vibration propagation, respectively. Selected electromagnetic parameters, including back-EMF, current, cogging torque, and starting torque, are analyzed and compared using finite element models developed in JMAG<sup>®</sup> [11], supported by selected analytic estimations. These findings are complemented by extensive experimental investigations into the vibration behavior of the drive based on an industrial vibration standard.

Following a brief introduction to single-phase claw-pole machines and their operating principles in Section III, the main part of this paper is structured into two parts: The first, spanning Sections IV and V, investigates four main claw geometries,  $D0$  through  $D3$ . Comparative analysis of these main geometries identifies the design exhibiting the most favorable vibration performance, laying the groundwork for further enhancements. Building on these results, the second part, presented in Sections VI and VII, extends the investigation to additional geometry modifications, focusing on

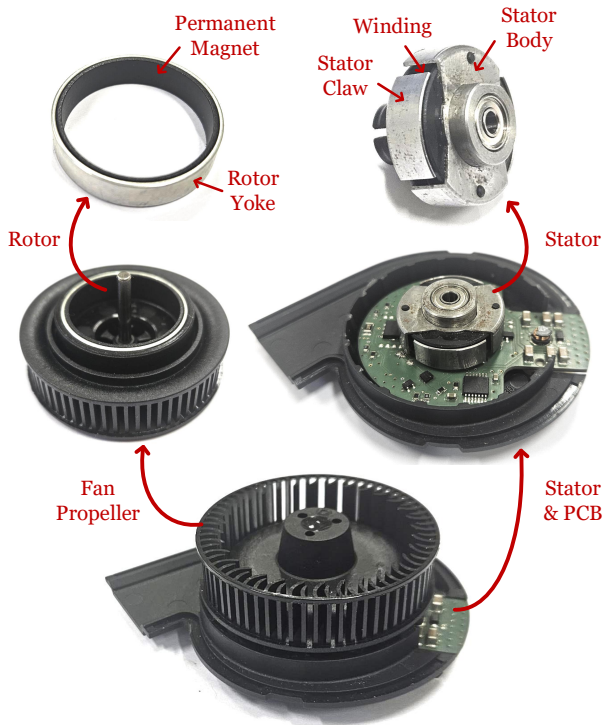


Fig. 1. Example case claw-pole single-phase BLDC fan drive.

TABLE I  
INVESTIGATED CLAW GEOMETRIES.

Design	Claw shape	Vibration analysis
$D_0$	Rectangular	Section V
$D_1$	Skewed claw	Section V
$D_2$	$D_1$ with auxiliary slot	Section V
$D_3$	Trapezoidal	Section V
$D_3'$	$D_3$ with reduced axial length	Section VII
$D_3''$	$D_3'$ with reduced axial length	Section VII
$D_4$	Asymmetric $D_3$	Section VII

three further claw-pole designs,  $D_3'$ ,  $D_3''$ , and  $D_4$ . Table I summarizes these designs. Each of these two parts comprises two main sections: First, the introduction of the designs and an analysis of their electromagnetic and structural parameters. Second, the presentation of the results of the experimental vibration analysis, providing a comparative assessment of the vibration performance of the investigated designs.

### III. CLAW-POLE SINGLE-PHASE BLDC FAN DRIVES

Fig. 1 illustrates an example case of a claw-pole single-phase BLDC motor configuration featuring an outer-rotor topology, employed in automotive fan applications. In contrast to the laminated stator in salient-pole electric machines, the stator of this claw-pole machine is made from a punched and bent solid iron sheet which leads to eddy current losses and thus lower efficiency compared to salient-pole machines. In this motor structure, the flux in the stator has a 3-dimensional path where the claws collect flux within the air-gap, channeling

TABLE II  
PARAMETERS OF THE EXAMPLE CASE FAN DRIVE.

Parameter	Value
DC link voltage ( $U_{DC}$ )	8 – 16 V
Nominal speed ( $\omega_{nom}$ )	5000 rpm
Phase resistance ( $R_{ph}$ )	8.5 $\Omega$
Stator outer diameter	23 mm
Stator sheet thickness	0.5 mm
Slot no. ( $S$ )	4
Pole-pair no. ( $p$ )	2
Magnet residual flux density ( $B_r$ )	0.36 T
Rotor stack length	6 mm
Stator sheet thickness	0.5 mm
Air-gap length	0.5 mm

it towards the stator body. The flux traverses through the central section of the stator before returning to the air-gap on the opposite side. In the example fan drive systems, the stator is integrated with the printed circuit board, which includes the inverter and control components. The stator winding in claw-pole machines is a ring-shaped winding, offering a simpler and more cost-effective winding process compared to salient-pole machines. The motor parameters are detailed in Table II.

### IV. MAIN CLAW GEOMETRIES: $D_0$ - $D_3$

With claw-pole single-phase BLDC motors, the claws have a central influence on both the electromagnetic and the structural performance of the motor: They directly interact with the permanent magnets guiding the flux that crosses the air-gap, thereby eventually influencing the back-EMF induced in the stator winding and thus the current requirement for a certain torque.

#### A. Investigated Claw Geometries

Fig. 2 shows the four different claw designs investigated in this study and indicates the parameters used to describe the structures. The values of these parameters are detailed in Table III. The conventional rectangular claw shape,  $D_0$ , is the baseline for the investigation.

The common technique of skewing comes at the price of reduced flux linkage but, for claw-pole stators, can be realized during the punching of stator sheets, as indicated above. As per [3], the optimal skewing angle for practical implementation, which provides a trade-off between cogging torque and flux linkage reduction for a single-phase BLDC claw-pole machine, is  $\alpha_{skw} = 30^\circ_{mech}$ , providing design  $D_1$ , see Fig. 2.

Adding an auxiliary slot shifts the fundamental frequency of the cogging torque. In the example case single-phase BLDC machine, the dominant harmonic of the force is at the 4<sup>th</sup> harmonic [5]. Shifting the main frequency of the cogging torque to the 8<sup>th</sup> harmonic can decrease the dominant harmonic of the vibration [3]. Fig. 2 shows the implementation of auxiliary slots in the skewed claw design,  $D_2$ . Optimally, the dimensions of the newly introduced slot-openings in  $D_2$  should match those of the primary slot-openings in  $D_1$  [3],

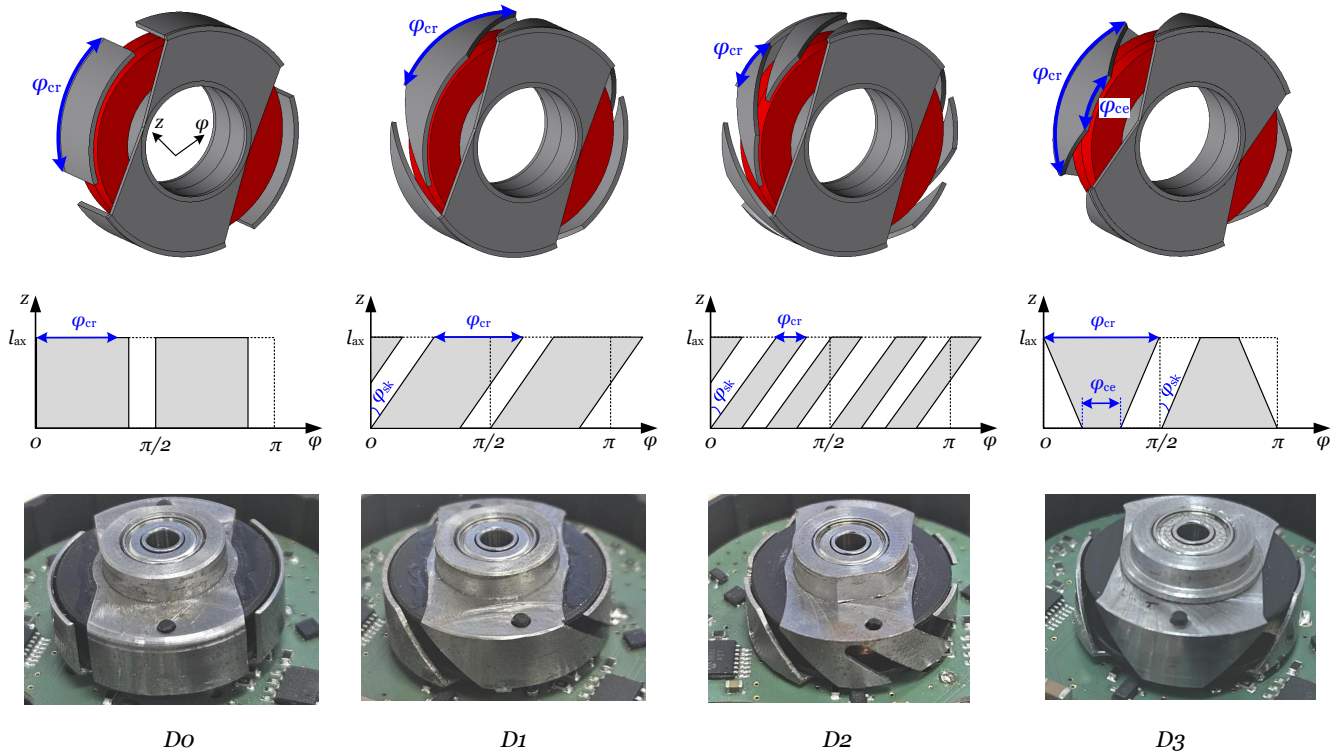


Fig. 2. Finite element models illustrated in JMAG<sup>®</sup>, drawing of the claws, and prototypes of stators with the main four different claw geometries: *D0*: rectangular claw, *D1*: skewed claw, *D2*: skewed claw with auxiliary slot, and *D3*: trapezoidal claw.

TABLE III  
DIMENSION OF INVESTIGATED MAIN CLAW GEOMETRIES *D0*-*D3*.

Design	Claw shape	Claw length ( $l_{ax}$ )	Claw-root angle ( $\varphi_{cr}$ )	Claw-end angle ( $\varphi_{ce}$ )	Skew angle ( $\varphi_{skw}$ )
<i>D0</i>	Rectangular	6 mm	72°	72°	-
<i>D1</i>	Skewed claw	6 mm	72°	72°	30°
<i>D2</i>	Skewed claw with auxiliary slot	6 mm	27°	27°	30°
<i>D3</i>	Trapezoidal	6 mm	90°	30°	30°

[12]. For design *D1*, with the pole pitch  $\tau_p$  and the claw-root angle  $\varphi_{cr}$ , the slot-opening angle  $\varphi_{so}$  is given by

$$\tau_p = \frac{360^\circ_{\text{mech}}}{2p} = 90^\circ_{\text{mech}}, \quad (1)$$

$$\varphi_{so} = \tau_p - \varphi_{cr,D1} = 18^\circ_{\text{mech}}, \quad (2)$$

From this, the claw-root angle of *D2* can be calculated by

$$\varphi_{cr,D2} = \frac{\varphi_{cr,D1} - \varphi_{so}}{2} = 27^\circ_{\text{mech}}. \quad (3)$$

Additionally, a symmetric trapezoidal claw shape, *D3*, is investigated, see Fig. 2. In the cases of *D0*-*D2*, the claw root angle,  $\varphi_{cr}$  must be smaller than the pole-pitch to limit the leakage flux by introducing the slot-opening. With the trapezoidal shaped claws, *D3*, the claw root angle can be theoretically larger, because the slot-opening can be implemented by introducing  $\alpha_{skw}$ , see Fig. 2. Still, as claw-root angles larger than the pole pitch are not recommended because

of the increase in leakage fluxes [2], it is chosen to equal the pole pitch,

$$\varphi_{cr,D3} = \tau_p = 90^\circ_{\text{mech}}. \quad (4)$$

When compared to the other designs, this design's larger claw root increases the active area to collect the magnetic flux, and thus increasing the linkage flux. Moreover, the wider claw root of *D3* increases the claw's stiffness. The skewing angle in *D3* is selected as  $\alpha_{skw} = 30^\circ_{\text{mech}}$  as a trade-off between increasing the linkage flux and the cogging torque compared to the baseline.

### B. Performance Analysis: *D0*-*D3*

1) *Cogging Torque Analysis*: Fig. 3 shows the cogging torque waveform of designs *D0* to *D3*. Skewing the claws in *D1* notably reduces the cogging torque's peak-to-peak value compared to *D0*. The spectrum of the cogging torque waveforms shows that skewing significantly decreases the two dominant harmonics, i.e., the 4<sup>th</sup> and the 12<sup>th</sup>. Adding an

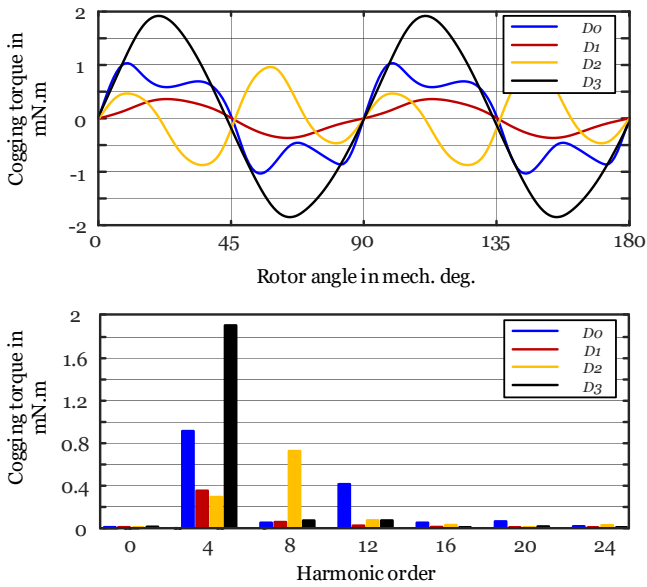


Fig. 3. Simulated cogging torque waveforms of the claw-pole machine with main claw geometries and their spectrum using JMAG®.

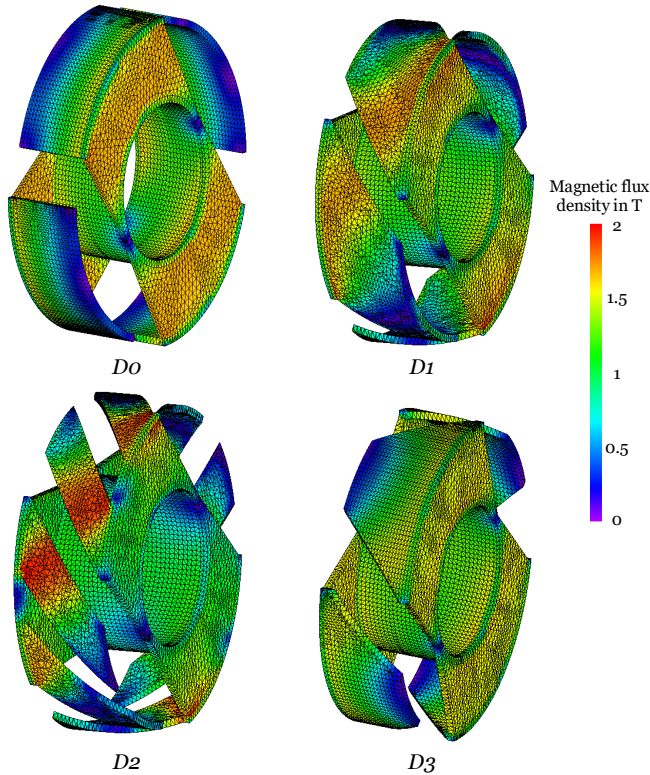


Fig. 4. Simulated magnetic flux density in the stator of claw-pole machine with main claw geometries using JMAG®.

auxiliary slot in  $D2$  also reduces the cogging torque's peak-to-peak value compared to  $D0$  while doubling its fundamental frequency. The amplitude of the 8<sup>th</sup> harmonic is increased, however, the main 4<sup>th</sup> harmonic is lower than in the case of  $D0$  and  $D1$ .  $D3$  shows a significantly increased cogging torque amplitude and main harmonic compared to the other designs.

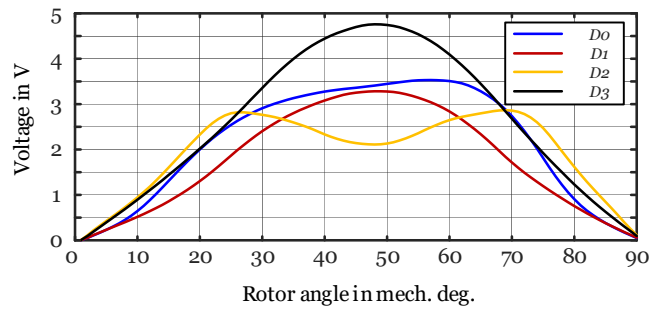


Fig. 5. Measured back-EMF waveform of claw-pole machine with main claw geometries.

However, the amplitude of the other harmonics is decreased compared to  $D0$ , which is mirrored in its sinusoidal waveform.

2) *Back-EMF Analysis*: Fig. 4 shows the magnetic flux density distributions in the stators. It demonstrates that in  $D0$  and  $D1$ , the flux density in the claw root and the stator body is higher than in the case of  $D3$ , due to the wider claw root of  $D3$ . With  $D2$ , saturation occurs in the claws due to the reduction of the flux path's active area.

Fig. 5 compares the measured back-EMF waveforms of the different designs at the machine's rated speed. As anticipated from Fig. 4, the trapezoidal design,  $D3$ , shows the highest back-EMF amplitude due to its wider claw root. On the other hand, when compared to  $D0$ , the skewing slightly reduces the voltage induced in the windings, because of the reduction of the flux linkage. The smaller effective cross-sectional area of the claws in  $D2$  also leads to a lower back-EMF amplitude compared to  $D1$ . The doubling of the fundamental harmonic by the introduction of the auxiliary slots is also evident in the back-EMF waveforms, see also Fig. 22(a).

3) *Mechanical Bending Analysis*: With the claw-pole machines, thinner stator claws allow for more pronounced bending, potentially increasing noise and vibration issues [13], [14]. This bending is determined by both the mechanical stiffness of the claw and the magnitude of the acting electromagnetic forces.

Given the flattened claw geometries illustrated in Fig. 6, the bending of the claws in  $z$  axis, can be computed as a function of  $x$  as [15]

$$\frac{\partial^2 z}{\partial x^2} = \frac{M(x)}{EJ_y}, \quad (5)$$

where  $E$ ,  $M$ , and  $J$  are Young's Modulus, the bending moment, and the area moment of inertia, respectively.

As derived in Appendix A, the bending line of the flattened rectangular claw in  $D0$  can be calculated as

$$z(x) = \frac{P}{2d^3 E} (6L^2 x^2 - 4Lx^3 + x^4), \quad (6)$$

where  $P$  is the uniform magnetic force density applied on the claw.

With the here investigated designs, the main geometrical parameter affecting the bending is the claws' length ( $L$ ). As per the theory, the claw thickness ( $d$ ) can also significantly affect the bending, but it has been kept constant across all the designs in this analysis.

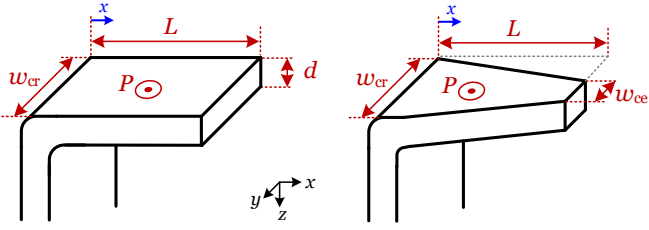


Fig. 6. Geometrical parameters of the claws  $D0$  and  $D3$  for mechanical bending analysis.

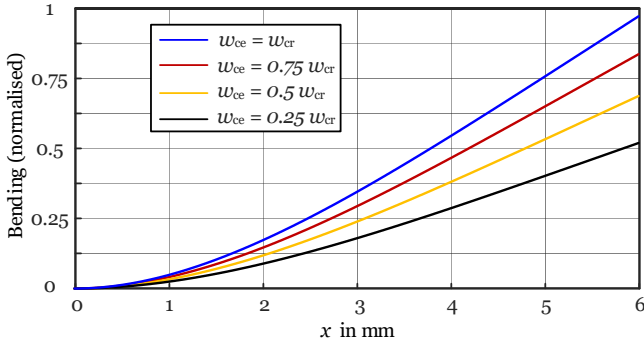


Fig. 7. Calculated claw deflection of rectangular ( $w_{ce} = w_{cr}$ ) and trapezoidal ( $w_{ce} \neq w_{cr}$ ) claw geometries.

Again, as derived in Appendix A, the bending line of the flattened trapezoidal claw in  $D3$  at position  $x$  can be computed by

$$z(x) = \frac{2P}{d^3 E} \left( L^2 \frac{x^2}{2} - L \frac{x^3}{3} + \frac{x^4}{12} + \dots \right. \\ \left. + 2Lw \left( L^2 \left( \left[ x + \frac{Lw_{cr}}{\Delta w} \right] (\ln(Lw_{cr} + x\Delta w) - 1) \right. \right. \right. \\ \left. \left. - x \ln(Lw_{cr}) - L \frac{w_{cr}}{\Delta w} (\ln(Lw_{cr}) - 1) \right) \right. \\ \left. + \left( \frac{1}{\Delta w} + \frac{2w_{cr}}{\Delta w^2} + \frac{w_{cr}^2}{\Delta w^3} \right) + \frac{x^3 - 6Lx^2}{6\Delta w} - \frac{Lw_{cr}x^2}{2\Delta w^2} \right). \quad (7)$$

where  $\Delta w = w_{ce} - w_{cr}$  to account for the non-uniform cross-section of the claw along the  $x$ -axis.

Fig. 7 compares the deflection of a trapezoidal claw for different  $w_{cr}$  and  $w_{ce}$ , assuming a constant magnetic force density acting on the claws. The results show that the bending along the  $x$ -axis increases as the values of  $w_{cr}$  and  $w_{ce}$  approach each other, i.e., the claws become more rectangular and less trapezoidal.

## V. VIBRATION ANALYSIS $D0$ - $D3$

BLDC machines typically require rotor position information to adjust the current polarity in the stator winding. In low-cost applications, single-phase BLDC machines use a Hall-effect sensor to provide this necessary position information. As illustrated in Fig. 8, the Hall-effect sensor detects the zero-crossing points of the back-EMF signal by generating rising or falling voltage edges. These edges serve as references for the determination of the advanced turn-off angle,  $\alpha_a$ , and delayed

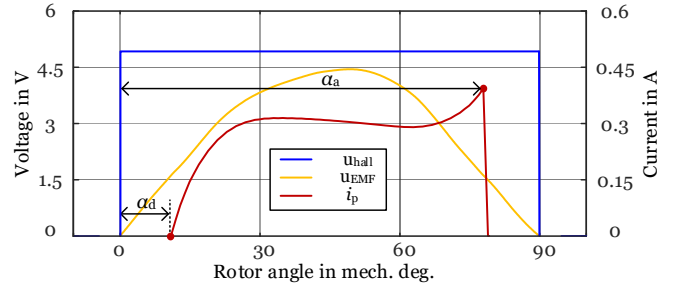


Fig. 8. Illustration of Hall-effect position signal ( $u_{hall}$ ) in relation to back-EMF signal ( $u_{EMF}$ ) zero-crossing points and phase current ( $i_p$ ) including the switching angles.

turn-on angle,  $\alpha_d$ . These angles are typically implemented to enhance motor efficiency and reduce vibration [16], [17].

### A. Preliminary Vibration Analysis

The vibration measurement setup used to experimentally assess the vibrations of the example case fan drives is shown in Appendix B. The vibration setup is based on an industrial standard [18], which also defines three force limits based on the specific application area of the drive (see Fig. 9).

Fig. 9 compares the measured vibrations of the example case drives occurring at the switching angles, optimized for best vibration performance based on [17]. Fig. 10 shows the currents measured at these operation points. Here, as the turn-on and -off switching angles have been set to minimize vibration, the machines' speeds are controlled by the DC input voltage.

The measurement results indicate that the forces generated by designs  $D0$  and  $D3$  can meet the requirements of the standard at their best vibration performance. However, generally,  $D3$  exhibits superior performance to  $D0$  across most of the frequency range. In contrast, designs  $D1$  and  $D2$  exceed the limitations defined by the standard at some harmonics.

As illustrated in Fig. 9, the force at 316 Hz corresponds to the main force harmonic, i.e., the 4<sup>th</sup> harmonic, at the rated speed of the motor. Moreover, 630 Hz and 1000 Hz correspond to the 8<sup>th</sup> and 12<sup>th</sup> force harmonic, respectively.

Summarizing the vibration performances of the different designs as identified by these measurement results:

- $D1$  and  $D0$ : As shown in Fig. 5, the back-EMF of  $D1$  is reduced compared to  $D0$ . Thus, more input current is required to maintain the constant output power of the fan drive at the rated speed. This is also evident in Fig. 10, where both the average and the maximum input currents of  $D1$  are higher compared to those of  $D0$ , leading to an increase in the 4<sup>th</sup> force harmonic. However,  $D1$  shows a reduced 12<sup>th</sup> force harmonic compared to  $D0$ .
- $D2$  with  $D1$ : Doubling the number of slots by adding an auxiliary slot in  $D2$  significantly increases the 8<sup>th</sup> force harmonic. This is due to the main harmonic of the pulsating magnetic forces which corresponds to the least common multiple of the slots and poles [5], which in this case is the 8<sup>th</sup> harmonic. Additionally, due to the larger width of the back-EMF of  $D2$  shown in Fig. 5, the

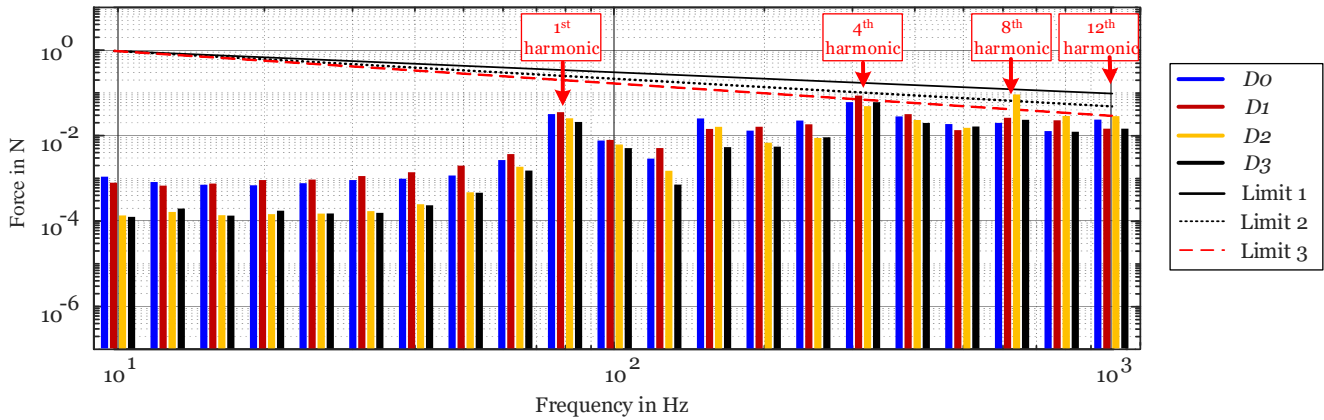


Fig. 9. Measured best vibration behavior of main claw geometries in one-third octave band analysis including the limits from the standard [18].

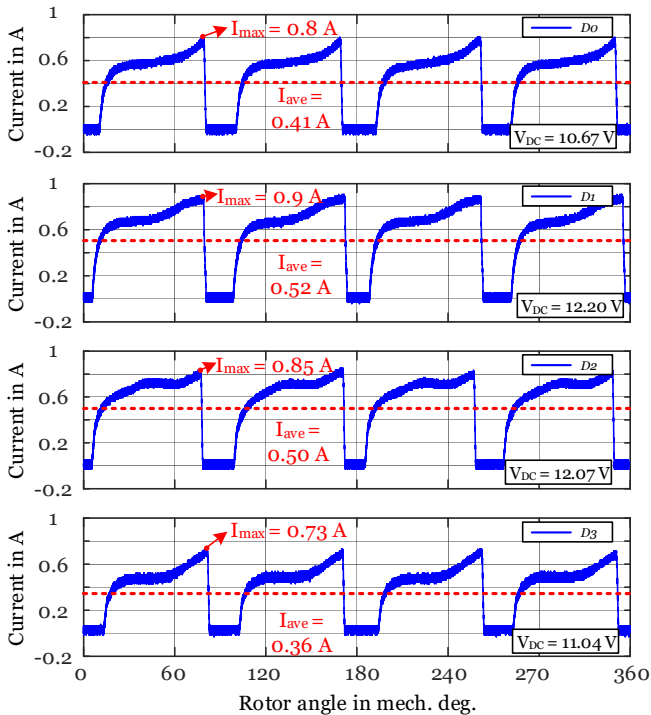


Fig. 10. Measured input current of best vibration behavior operating switching angles of main claw geometries.

maximum input current, which occurs close to the zero-crossing points of the back-EMF, is reduced compared to *D1*. This can increase the efficiency in this specific operating point.

- *D3* with *D0*: A comparison of the current consumption of these designs in Fig. 10 shows that the average and peak current values are reduced in *D3* compared to *D0*. This is due to the higher fundamental harmonic of the back-EMF in *D3*. Therefore, although both designs can meet the standard at this operating point, the force harmonics of *D3* are overall lower than those of *D0*.

TABLE IV  
MEASURED INPUT POWER: *D0*-*D3*.

Claw design	Average $P_{in}(W)^*$	Average $P_{in}(W)^{**}$
<i>D0</i>	4.62	4.79
<i>D1</i>	6.73	—
<i>D2</i>	6.58	—
<i>D3</i>	3.99	4.32

\*: Average input power in all operation points in Fig. 11.

\*\* : Average input power in hatched area in Fig. 11.

### B. Comprehensive Vibration Analysis

The preliminary vibration analysis compared the vibration of four main claw geometries at the respective sets of switching angles leading to the best vibration performances per design. To compare these motors across a wider range of switching angles,  $\alpha_d$  and  $\alpha_a$  have been varied from  $5^\circ_{mech}$  to  $15^\circ_{mech}$  and from  $60^\circ_{mech}$  to  $85^\circ_{mech}$ , respectively. The turn-on angle cannot be below  $5^\circ_{mech}$ , and the turn-off angle cannot exceed  $85^\circ_{mech}$ , due to constraints imposed by the limit of calculation power of the microprocessor.

The measurement results for the four aforementioned geometries at the three main dominant harmonics, i.e., the 4<sup>th</sup>, the 8<sup>th</sup>, and the 12<sup>th</sup>, are depicted in Fig. 11. Furthermore, Limit 3 from the standard is also shown for each harmonic to facilitate the comparison of the measured values with the standard. The hatched area in each sub-figure indicates the areas where all limits are met at least for one  $\alpha_d$  value. In addition, Table IV shows the measured input power of the fan drives.

As per these results, the most critical harmonic for all claw geometries is the 12<sup>th</sup>. This is explained by a resonance in the mechanical structure near this frequency which was detected in a run-up test described in Appendix C. The variation of this force harmonic is highly affected by the current harmonics, as described both analytically and experimentally in [17].

Summarizing the vibration performances of the different designs as identified by these comprehensive measurement results:

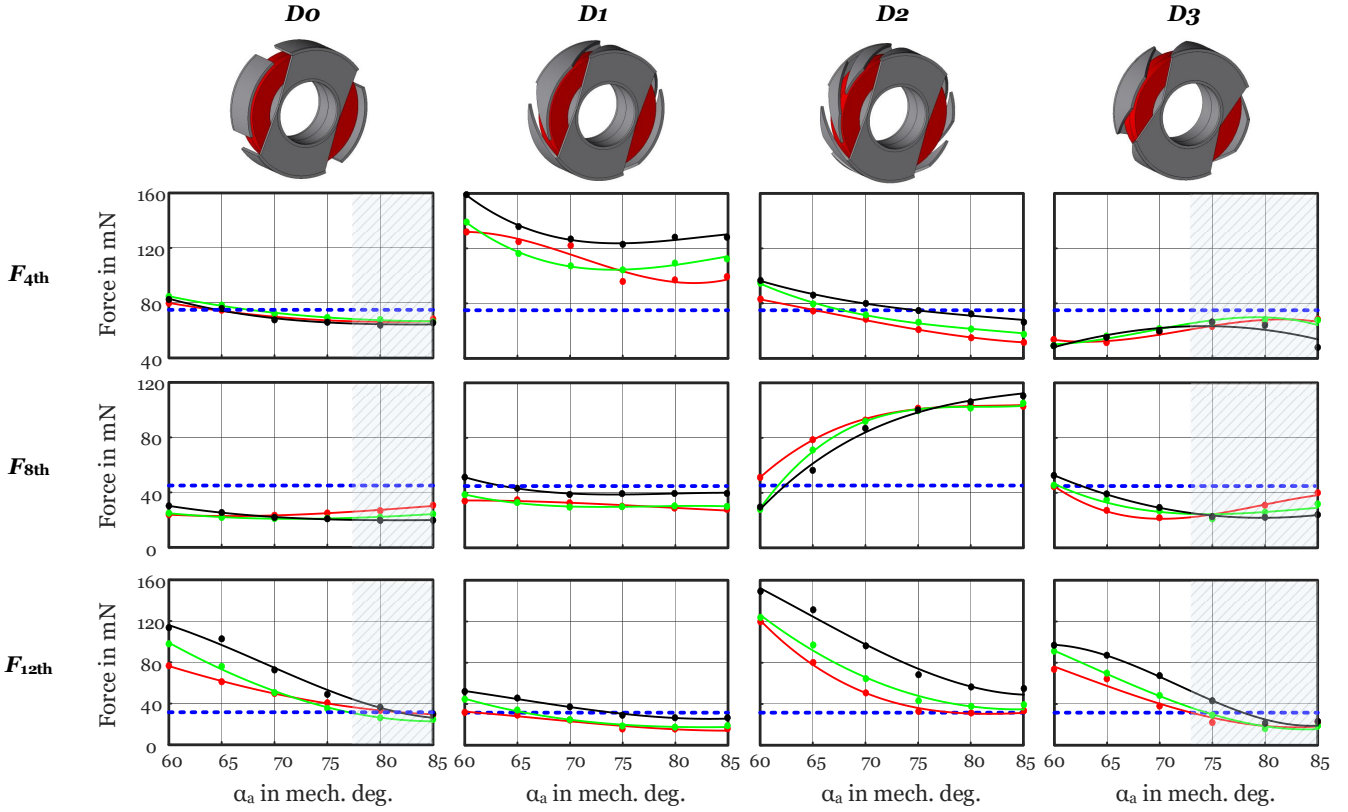


Fig. 11. Measured main vibration harmonics of the claw-pole single-phase BLDC fans with main claw geometries at the nominal speed including switching angle variations. Blue: limit based on the standard; red: turn-on angle at  $\alpha_d = 5^\circ_{\text{mech}}$ ; green: turn-on angle at  $\alpha_d = 10^\circ_{\text{mech}}$ ; black: turn-on angle at  $\alpha_d = 15^\circ_{\text{mech}}$ , and hatched area: the area where all the limits are satisfied at least for one  $\alpha_d$ .

- *D0*: The vibration of design *D0* can only remain below the limit of the 12<sup>th</sup> harmonic for  $\alpha_a$  angles greater than  $75^\circ_{\text{mech}}$ . Except for the high 4<sup>th</sup> harmonic at low  $\alpha_a$ , which is due to the high input current from the short conduction period, other harmonics demonstrate acceptable performance across the entire range of switching angles. Therefore, the range in which this design can satisfy the standard is limited to  $\alpha_a$  angles greater than  $75^\circ_{\text{mech}}$ .
- *D1*: Implementing skewing to the rectangular claw shape reduces the 12<sup>th</sup> harmonic across a wide range of switching angles. Nevertheless, as the effective flux linkage in the motor decreases, more input power is required to drive the fan. This increases the 4<sup>th</sup> force harmonic, which remains above the limit for the entire set of switching angles. The increase in input current for this design is also observed in Table IV, and the motor's input power is significantly higher than that of *D0*.
- *D2*: *D2* reduces the 4<sup>th</sup> force harmonic compared to *D1*. However, the 8<sup>th</sup> harmonic shows a significant increase, surpassing the allowed limit for almost all sets of switching angles. This increase, as predicted earlier, is attributed to the doubling of the number of slots. *D2* only marginally remains below the standard limit for a few sets of switching angles when  $\alpha_d = 5^\circ_{\text{mech}}$  at the 12<sup>th</sup> harmonic. This design cannot satisfy the standard limit for all force harmonics. The input power is slightly reduced compared to *D1* due to the wider back-EMF,

which reduces the current peak as previously shown in Fig. 10.

- *D3*: *D3* shows better performance at the 12<sup>th</sup> force harmonic compared to other designs, and it can meet the standard requirements for a wider range of switching angles. Additionally, the other two main harmonics, 4<sup>th</sup> and 8<sup>th</sup>, remain below the limits for almost the entire range of switching angles. Considering the input powers, *D3* shows the lowest energy consumption among the different designs. This reduction is attributed to the higher back-EMF, as demonstrated for the current at optimal vibration switching angles in Fig. 10.

The overall performance comparison among these designs indicates that the trapezoidal claw shape, *D3*, exhibits a better vibration performance and higher efficiency than the other designs across a wide range of operated switching angles. Thus, this design is selected for additional investigations aimed at further enhancing vibration performance.

## VI. FURTHER GEOMETRY ANALYSIS: *D3* VARIATIONS AND *D4*

### A. Axial Length Variation of *D3*

In the case of the main claw geometries discussed in Section IV and V, the axial length of the claws was equal to that of the permanent magnet in the rotor. However, due to the unique flux path of these machines, not the entire axial cross-section of the claw equally contributes to torque production.

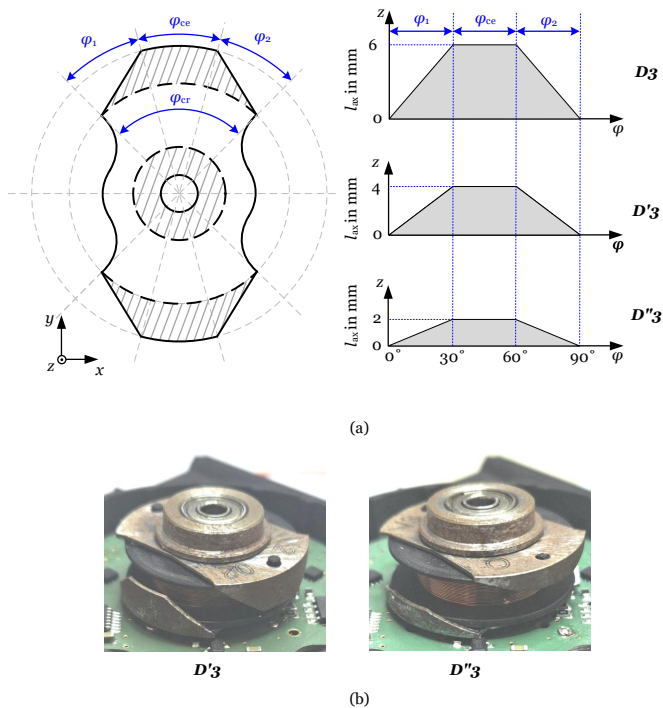


Fig. 12. The claw-pole machine with trapezoidal claw,  $D_3$ , with different axial lengths of the claw: (a) drawings of the claw shapes and (b) prototypes.

As shown in Fig. 4, the magnetic flux density decreases with distance from the claw root. Since also the length of the claws significantly impacts the claw bending, the possibility of axial length reduction is investigated, where reduced lengths are expected to result in stiffer claws, but bending may increase due to the increase of current required to operate at the desired torque.

To this aim, two additional claw-pole motors with trapezoidal claws and reduced axial lengths of 4 mm and 2 mm, respectively,  $D_3'$  and  $D_3''$ , are designed, as shown in Fig. 12.

1) *Cogging Torque Analysis*: Fig. 13(a) compares the simulated cogging torque of both claws with reduced axial lengths. As the active area of the claw facing the permanent magnet in the air gap decreases with the reduction in axial length, the cogging torque also decreases. Specifically, the peak-to-peak value of the cogging torque for  $D_3'$  and  $D_3''$  is reduced by 30% and 58%, respectively, compared to  $D_3$ .

2) *Back-EMF Analysis*: Fig. 13(b) compares the back-EMF of these designs. Despite the reduction of the claw length by 33% and 67% for  $D_3'$  and  $D_3''$ , respectively, the peak value of the back-EMF decreases only by 24% and 51%. Additionally, the fundamental harmonic of the back-EMF experiences a reduction of 19% and 47%, respectively (see Fig. 22(b)), which is less than the reduction in claw length.

3) *Mechanical Bending Analysis*: The bending of designs  $D_3'$  and  $D_3''$  with reduced axial lengths is compared with design  $D_3$  by the bending equation of the trapezoidal claw shape in (7). Fig. 13(c) shows the normalized calculated bending of these claws under an assumed magnetic force density, confirming that reducing the axial lengths in  $D_3'$  and  $D_3''$  considerably increases the claws' stiffness and thus, at

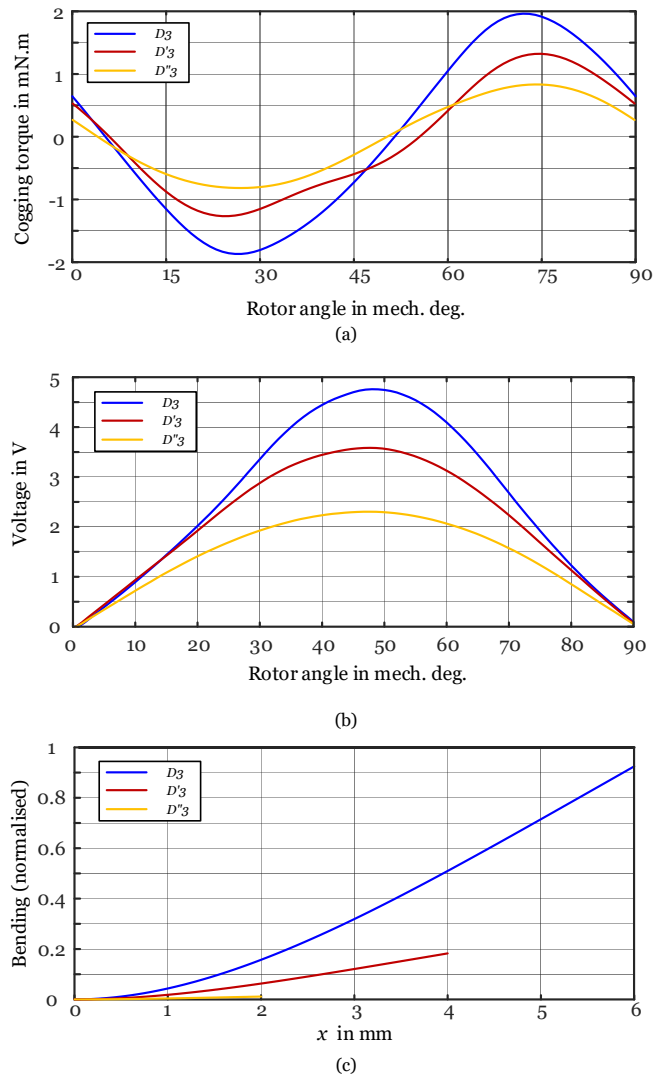


Fig. 13. Comparison between trapezoidal claw-pole with reduced axial length: (a) simulated cogging torque waveform in JMAG®, (b) measured back-EMF waveform, and (c) calculated claw deflection.

constant external force, decreasing the bending.

### B. Air-Gap Profile Variation

The stators of single-phase BLDC machines can only produce a pulsating magnetic field and are thus typically realized with an asymmetric air-gap. Thereby, an asymmetric magnetic flux density distribution along the air-gap is obtained, enabling the generation of a starting torque in a specific direction, e.g., [19], [20]. This has also been applied to all the previously investigated designs, see Fig. 14(a) for an exemplary illustration. Note the shifting of the center of the claw root's arc from  $I$  to  $I'$  by a distance  $d_{\text{asym}}$ . This asymmetric air-gap profile can generate starting torque in the clockwise direction.

Such asymmetric flux density distribution can also be obtained by an asymmetric claw shape with uniform air-gap length, as shown in Fig. 14(b). Here,  $\varphi_1$  is larger than  $\varphi_2$  ( $\varphi_1 = 45^\circ_{\text{mech}}$  and  $\varphi_2 = 15^\circ_{\text{mech}}$ ), which alters the flux density distribution in the air-gap and generates starting torque.

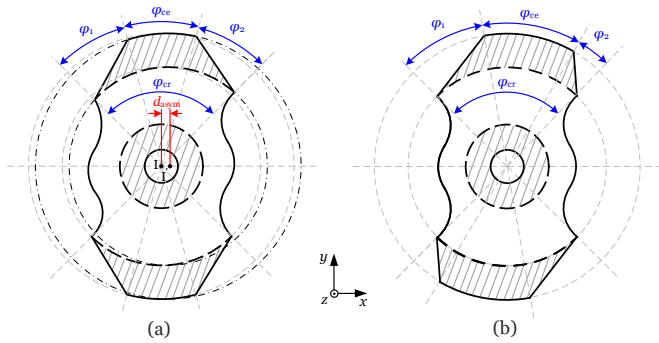


Fig. 14. Drawing of claw designs to implement asymmetric air-gap profile in claw-pole single-phase BLDC machines (solid lines indicate the punching lines and dashed lines indicate bending lines): (a) trapezoidal claw with tapered asymmetric air-gap and (b) asymmetric trapezoidal claw.

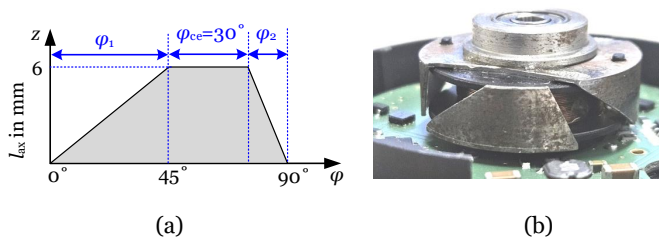


Fig. 15. Claw-pole single-phase fan drive with asymmetric trapezoidal shape, D4: (a) drawing of the claw shape with dimensions and (b) a prototype of the stator.

These angles have been selected by design-studies as a trade-off between the angle at which the back-EMF peaks (see Fig. 16(b)) and thus influencing the current peak at turn-off angle, and the back-EMF peak, both eventually influencing the current requirement, thus the electromagnetic forces and the vibration behavior. Fig. 15 shows the realized claws' profile and the prototype of the asymmetric trapezoidal claw geometry, D4.

1) *Cogging Torque Analysis*: Fig. 16(a) shows the cogging torque waveforms of the two designs, D3 and D4. The peak-to-peak cogging torque value of D4 is reduced by 15% compared to D3. Additionally, the zero-crossing points of the cogging torque waveform are shifted by approximately  $5^\circ_{\text{mech}}$ , which changes the rotor's standstill position and can impact the starting torque.

2) *Starting Torque Analysis*: The electromagnetic torque generated at the standstill position of the rotor equals the starting torque of this machine [21]. As per Fig. 16(b), design D4 can generate starting torque even at the absence of a tapered air-gap. At an input current of  $I_{DC} = 1.5 \text{ A}$ , corresponding to the current at the nominal voltage of the battery at standstill, the starting torque of D4 is 78% higher than the one of D3.

3) *Back-EMF Analysis*: Fig. 16(c) compares the measured back-EMF of designs D3 and D4. The peak of the back-EMF of D4 is shifted by approximately  $6^\circ_{\text{mech}}$  due to the asymmetric claw shape. The spectrum of the back-EMF signal shown in Appendix D reveals that in D4, the fundamental harmonic is reduced by 0.7%, while the third harmonic is increased by

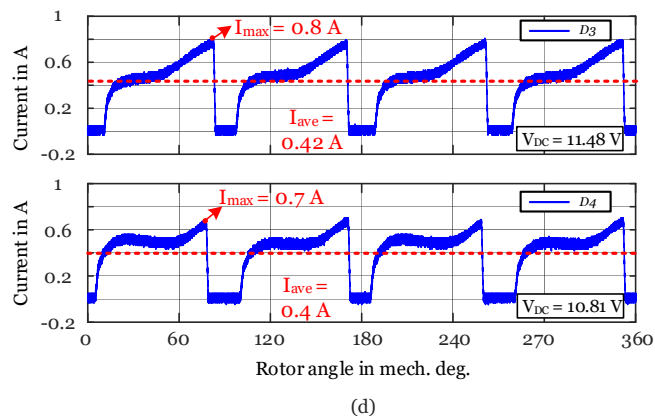
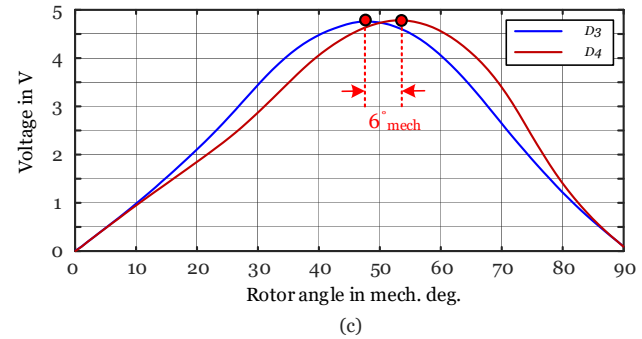
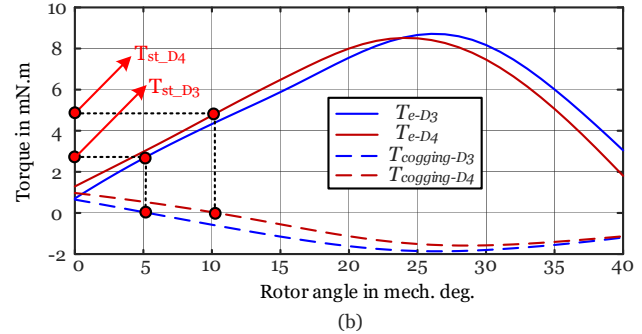
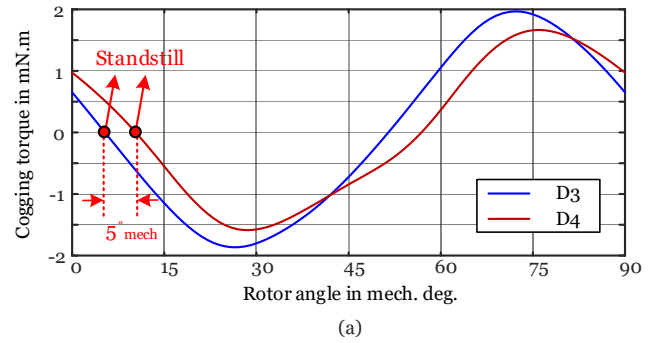


Fig. 16. Comparison between different asymmetric air-gap designs: (a) simulated cogging torque waveform in JMAG<sup>®</sup>, (b) simulated torque in JMAG<sup>®</sup> ( $T_{\text{cog}}$ ,  $T_e$ , and  $T_{\text{st}}$  are cogging torque, electromagnetic torque, and starting torque respectively), (c) measured back-EMF waveform, and (d) measured current at  $\alpha_d = 10^\circ_{\text{mech}}$  and  $\alpha_a = 85^\circ_{\text{mech}}$ .

24%.

The back-EMF shape of D4 results in a decreased peak current during operation at high  $\alpha_a$  angles. This is illustrated in Fig. 16(d), which compares the measured input current of both designs at  $\alpha_d = 10^\circ_{\text{mech}}$  and  $\alpha_a = 85^\circ_{\text{mech}}$ . It is

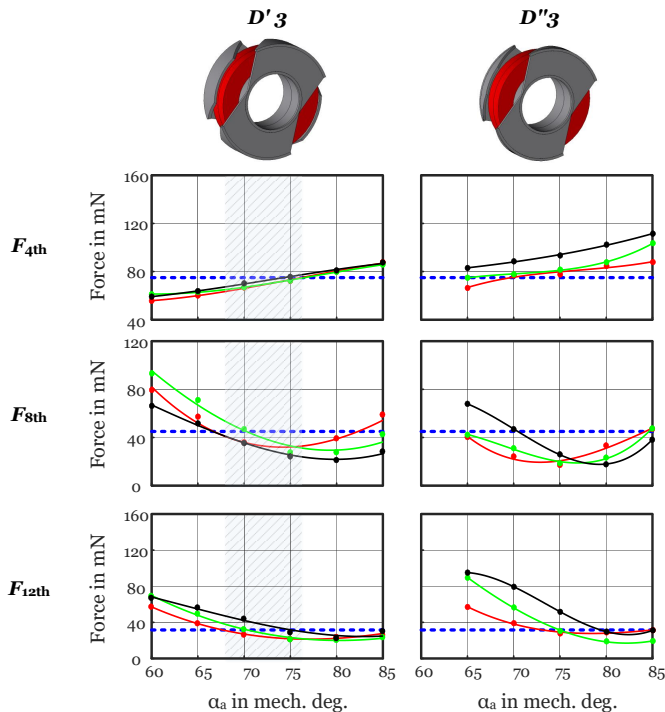


Fig. 17. Measured main vibration harmonics of the claw-pole single-phase BLDC fans with  $D3$  claw geometry with reduced claw length ( $D3'$  and  $D3''$ ) at the nominal speed including switching angle variations. Blue: limit based on the standard; red: turn-on angle at  $\alpha_d = 5^\circ_{\text{mech}}$ ; green: turn-on angle at  $\alpha_d = 10^\circ_{\text{mech}}$ ; black: turn-on angle at  $\alpha_d = 15^\circ_{\text{mech}}$ , and hatched area: the area where all the limits are satisfied at least for one  $\alpha_d$ .

TABLE V  
MEASURED INPUT POWER:  $D3$  VARIATIONS AND  $D4$ .

Claw design	Average $P_{\text{in}}$ (W)*	Average $P_{\text{in}}$ (W)**
$D3$	3.99	4.32
$D3'$	4.43	4.79
$D3''$	7.42	-
$D4$	4.12	4.13

\*: Average input power in all operation points in Fig. 17-18.

\*\*: Average input power in hatched area in Fig. 17-18.

evident that while the first current peak of  $D4$  is higher than that of  $D3$ , the second peak is significantly lower. Since the second current peak does not significantly contribute to the torque development, the input current of  $D4$  is lower. At this operational point, taking into account the measured DC voltage values in Fig. 16(d), the input power of  $D4$  is measured at 4.32 W, which is less than the 4.82 W recorded for  $D3$ .

## VII. VIBRATION ANALYSIS: $D3$ VARIATIONS AND $D4$

### A. Vibration Analysis: Axial Length Variations of $D3$

A comprehensive vibration analysis of the fan drives with axial length variations of  $D3$ ,  $D3'$ , and  $D3''$ , is presented in Fig. 17. As anticipated from the back-EMF comparison, the input power of the fan drive, shown in Table. V, has increased for both designs with reduced claw lengths, compared to  $D3$ , with the increase being more significant for  $D3''$  than for  $D3'$ .

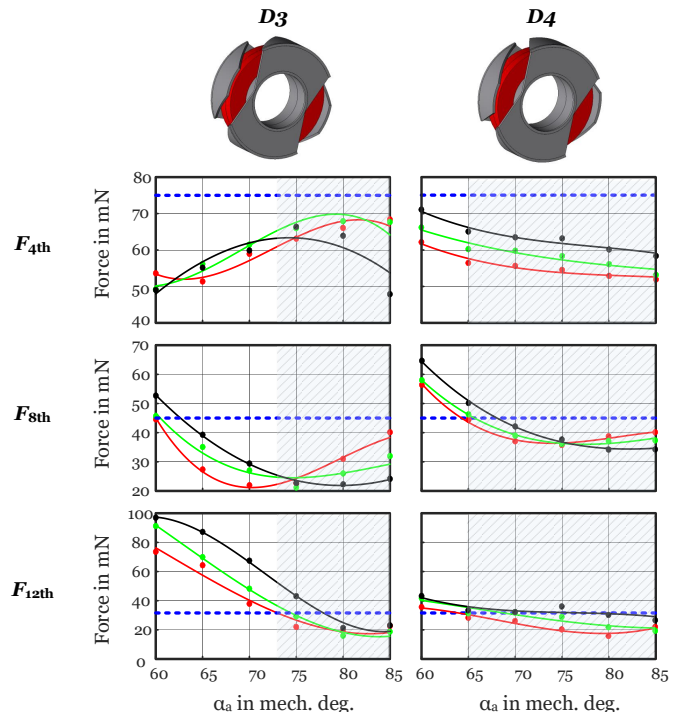


Fig. 18. Measured main vibration harmonics of the claw-pole single-phase BLDC fans with  $D3$  and  $D4$  claw geometry at the nominal speed including switching angle variations. Blue: limit based on the standard; red: turn-on angle at  $\alpha_d = 5^\circ_{\text{mech}}$ ; green: turn-on angle at  $\alpha_d = 10^\circ_{\text{mech}}$ ; black: turn-on angle at  $\alpha_d = 15^\circ_{\text{mech}}$ , and hatched area: the area where all the limits are satisfied at least for one  $\alpha_d$ .

The increase in required input power, bringing forth a higher input current at constant voltage, results in an increase in the 4<sup>th</sup> force harmonic. This force surpasses the standard limit at almost  $75^\circ_{\text{mech}}$  for  $D3'$  and above  $70^\circ_{\text{mech}}$  for  $D3''$ . At the 12<sup>th</sup> harmonic,  $D3'$  outperforms  $D3$  and meets the requirement for a wider range of operating points. However, this improvement is not observed for  $D3''$ .

The overall comparison shows that although  $D3'$  performs better than  $D3$  at the 12<sup>th</sup> harmonic, the range in which it can meet the limit for all harmonics is more restricted than  $D3$ . These results indicate that although the bending of the claws was significantly reduced by decreasing their axial lengths, the overall vibration performance of  $D3'$  and  $D3''$  did not improve compared to  $D3$ . This is due to the increased electromagnetic forces associated with the higher current in the stator winding.

Optimization of both the claw-end angle and the axial length may identify an optimum combination, which may be a subject of further research.

### B. Vibration Analysis: Air-gap Profile Variation

Fig. 18 compares the main vibration harmonics of  $D3$  and  $D4$ , where vibration performance of  $D4$  is significantly improved compared to  $D3$ . Specifically, the operating range where all main harmonics comply with the standard limit is increased, as indicated by the hatched area in Fig. 18. For instance, at  $\alpha_d = 5^\circ_{\text{mech}}$ , all harmonics for  $D4$  are below the limit when  $\alpha_a > 65^\circ_{\text{mech}}$ , whereas for  $D3$ , this occurs when  $\alpha_a > 75^\circ_{\text{mech}}$ .

TABLE VI  
OVERALL COMPARISON OF ALL INVESTIGATED CLAW GEOMETRIES AT NOMINAL SPEED.

Design	Claw shape	Satisfying Vibration Standard	Vibration Level	Input Power
$D0$	Rectangular	●	● ● ● ○	● ● ○ ○
$D1$	Skewed claw	●	● ● ● ●	● ● ● ○
$D2$	Skewed claw with auxiliary slot	●	● ● ● ●	● ● ● ○
$D3$	Trapezoidal - 6 mm	●	● ● ○ ○	● ○ ○ ○
$D3'$	Trapezoidal - 4 mm	●	● ● ● ○	● ● ○ ○
$D3''$	Trapezoidal - 2 mm	●	● ● ● ●	● ● ● ●
$D4$	Asymmetric trapezoidal	●	● ○ ○ ○	● ○ ○ ○

The efficiency of  $D4$  is also improved in comparison to  $D3$  in the region where the vibration standard is met, as shown in Table V. This improvement is due to the lower current peak observed at these angles. However, due to the reduced back-EMF at low  $\alpha_a$  switching angles, both the input current and power increase for  $D4$  relative to  $D3$ , resulting in a higher overall average input power for  $D4$ .

### VIII. CONCLUSION

This paper shows an extensive analysis of the impact of different claw geometries on the vibration characteristics of small single-phase claw-pole BLDC motors across a wide range of operating points.

The study initially compares four main claw geometries: conventional rectangular ( $D0$ ), skewed ( $D1$ ), skewed with auxiliary slot ( $D2$ ), and trapezoidal ( $D3$ ) claw shapes, through finite element simulations, analytic mechanical stiffness analysis, and extensive experimental investigations. The results demonstrate that the motor with a trapezoidal claw shape exhibits the best overall performance in terms of vibration and required input power.

Then, this study also investigates designs with different axial claw lengths and design options to obtain the necessary asymmetric flux-density distribution. The results show reducing the axial length of the claw does not improve the vibration performance because of the increase of current requirement and thus force. However, implementing an asymmetric trapezoidal claw shape,  $D4$ , improves both the vibration performance and the efficiency.

Table VI qualitatively summarizes the performances of the different geometries.

### ACKNOWLEDGMENT

The financial support by the Austrian Federal Ministry of Labour and Economy, the National Foundation for Research, Technology and Development and the Christian Doppler Research Association is gratefully acknowledged. The authors also would like to express their appreciation to Dr. Felix Krall and Dr. Stefan Leitner for their valuable contributions during the design and prototyping stages. The authors are also thankful to MSG Mechatronic Systems GmbH, Wies, Austria for manufacturing the stator parts.

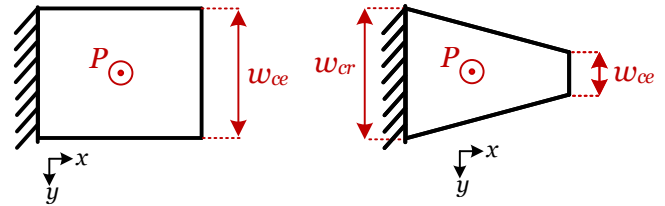
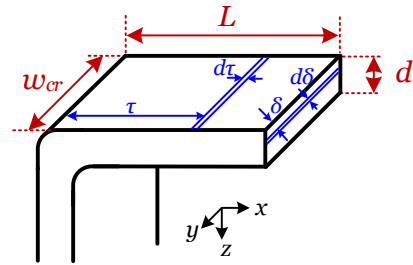


Fig. 19. Drawing of the claws to calculate the bending equation.

### APPENDIX A BENDING EQUATION DERIVATION

#### A. Rectangular Claw

For the rectangular shape claw, as shown in Fig. 19, the claw's width is constant across  $x$  axis. Therefore the width of the beam at position  $x$  is

$$w(x) = w = w_{cr}; (w_{cr} = w_{ce}). \quad (8)$$

The area-moment of inertia and the bending moment can be calculated as

$$J_y(x) = J_y = 2 \int_0^{\frac{d}{2}} \delta^2 w_{cr} d\delta = w_{cr} \frac{d^3}{12}, \quad (9)$$

$$M(x) = \int_{\tau=x}^L (\tau - x) p w_0 d\tau = P w_{cr} \frac{(L - x)^2}{2}, \quad (10)$$

where  $P$  is the uniform magnetic force density applied on the claw.

The second derivative of the bending line at position  $x$  is

$$\frac{\partial^2 z}{\partial x^2} = \frac{M(x)}{E J_y}, \quad (11)$$

where  $E$  is the Young's Modulus.

By substituting (9) and (10) in (11), this can be written as

$$\frac{\partial^2 z}{\partial x^2} = \frac{12P}{d^3 E} \frac{w_{cr}(L-x)^2}{2w_{cr}} = \frac{6P}{d^3 E} (L-x)^2. \quad (12)$$

The bending line can be calculated as

$$\begin{aligned} z(x) &= \frac{6P}{d^3 E} \left( \frac{L^2}{2} x^2 - \frac{L}{3} x^3 + \frac{1}{12} x^4 \right) \\ &= \frac{P}{2d^3 E} (6L^2 x^2 - 4Lx^3 + x^4). \end{aligned} \quad (13)$$

### B. Trapezoidal Claw

As shown in Fig. 19, the width of the trapezoidal claw across  $x$  is not constant. It can be written as

$$w(x) = w_{cr} + x \frac{\Delta w}{L}, \quad (14)$$

where  $\Delta w$  is  $w_{ce} - w_{cr}$ .

The area-moment of inertia and the bending moment can be calculated as

$$\begin{aligned} J_y(x) &= 2 \int_0^{\frac{\Delta}{2}} \delta^2 w(x) d\delta = w(x) \frac{d^3}{12} \\ &= \left[ w_{cr} + x \frac{\Delta w}{L} \right] \frac{d^3}{12}, \end{aligned} \quad (15)$$

$$\begin{aligned} M(x) &= \int_{\tau=0}^{L-x} \tau P w(x + \tau) d\tau \\ &= P \int_{\tau=0}^{L-x} \tau \left[ w_{cr} + (x + \tau) \frac{\Delta w}{L} \right] d\tau \\ &= P \left[ \frac{\tau^2}{2} \left( w_{cr} + x \frac{\Delta w}{L} \right) + \frac{\tau^3}{3} \frac{\Delta w}{L} \right]_{\tau=0}^{L-x} \\ &= P \frac{(L-x)^2}{6} \left[ 3w_{cr} + 3x \frac{\Delta w}{L} + 2(L-x) \frac{\Delta w}{L} \right] \\ &= P \frac{(L-x)^2}{6} \left[ w_{cr} + 2w_{ce} + x \frac{\Delta w}{L} \right] \\ &= P \frac{(L-x)^2}{6} [2w_{ce} + w(x)]. \end{aligned} \quad (16)$$

The second derivative of the bending line at position  $x$  can be calculated from (11) as

$$\begin{aligned} \frac{\partial^2 z}{\partial x^2} &= \frac{12P}{d^3 E} \frac{(L-x)^2}{6w(x)} [2w_{ce} + w(x)] \\ &= \frac{2P}{d^3 E} (L-x)^2 \left[ 2 \frac{w_{ce}}{w(x)} + 1 \right] \\ &= \frac{2P}{d^3 E} \left[ (L-x)^2 + 2Lw_{ce} \frac{(L-x)^2}{Lw_{cr} + x\Delta w} \right]. \end{aligned} \quad (17)$$

Therefore, the bending line at position  $x$  is

$$\begin{aligned} z(x) &= \frac{2P}{d^3 E} \left( L^2 \frac{x^2}{2} - L \frac{x^3}{3} + \frac{x^4}{12} + \dots \right. \\ &\quad + 2Lw_L \left( L^2 \left( \left[ x + \frac{Lw_{cr}}{\Delta w} \right] (\ln(Lw_{cr} + x\Delta w) - 1) \right. \right. \\ &\quad \left. \left. - x \ln(Lw_{cr}) - L \frac{w_{cr}}{\Delta w} (\ln(Lw_{cr}) - 1) \right) \right. \\ &\quad \left. + \left( \frac{1}{\Delta w} + \frac{2w_{cr}}{\Delta w^2} + \frac{w_{cr}^2}{\Delta w^3} \right) + \frac{x^3 - 6Lx^2}{6\Delta w} - \frac{Lw_{cr}x^2}{2\Delta w^2} \right). \end{aligned} \quad (18)$$

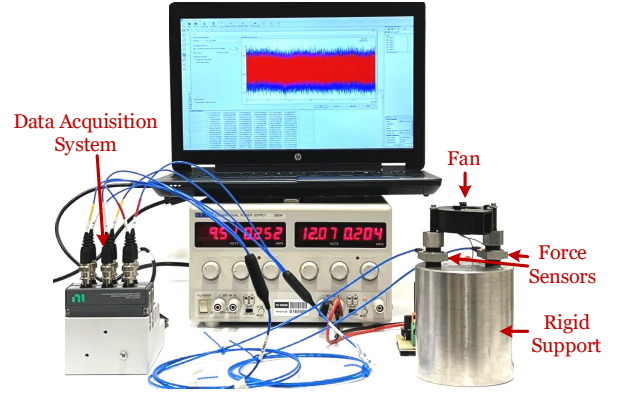


Fig. 20. Vibration measurement setup.

## APPENDIX B

### STANDARD VIBRATION MEASUREMENT SETUP

The example case drive utilized for experimental investigations is a fan drive designed for automotive applications, equipped with a single-phase claw-pole BLDC motor. To assess the vibration characteristics of different designs, an experimental setup based on an industrial standard [18] has been employed which is one of the few industrial standards for noise and vibration of small electric drives. The measurement setup involves two triaxial force sensors, 260M36 model from PCB Piezotronics [22], and the fan system is mounted on a rigid support that is significantly heavier than the fan drive, as depicted in Fig. 20. The sensors' data are collected with a high precision data acquisition hardware cDAQ-9174 [23] with two NI-9232 measurement cards [24] from National Instruments.

According to the standard, all forces from all attachment points are summed up and represented in a one-third octave band spectrum, see Fig. 9. This standard also defines the allowed vibration values for auxiliary applications in the automotive industry with three limit curves, depending on the specific area of application in a car, as described in [18]:

- Limit 1: passenger-operated auxiliary device which is activated when the combustion engine is *on*.
- Limit 2: passenger-operated auxiliary device which is activated when the combustion engine is *off* and those which operate automatically when the combustion engine is *on*.
- Limit 3: automatic auxiliary device when the combustion engine is *off*.

## APPENDIX C

### NATURAL FREQUENCY ANALYSIS

Resonance between electromagnetic forces and the natural frequencies of the mechanical structure is one of the main sources of noise and vibration in electric machines. To identify the natural frequencies of the example case fan drive, vibration measurements are conducted during the motor's run-up test. The result of this experiment is presented in the spectrograms shown in Fig. 21. The measurement is performed at a standard

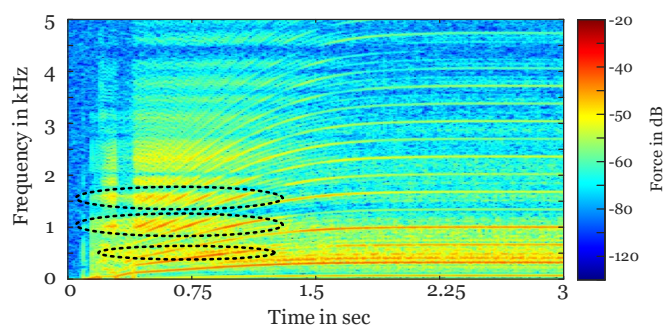


Fig. 21. Extraction of the natural frequencies of  $D1$  through run-up test.

sampling frequency of 51.2 kHz, and the spectrogram is generated using a Hanning window with a 75% overlap. Several resonances with the natural frequencies of close to 500, 1000, and 1500 Hz are consistently observed in the spectrogram, resonating with multiple magnetic force harmonics upon crossing these frequencies.

Due to the small mechanical dimension of these claw-pole motors, the natural frequencies of the stator and rotor occur at high frequencies and usually above the audible frequency range [5]. Therefore, the natural frequencies marked with dashed-line in Fig. 21 are related to the casing of the fan and appear in the spectrogram of all investigated fan drives with different claw geometries.

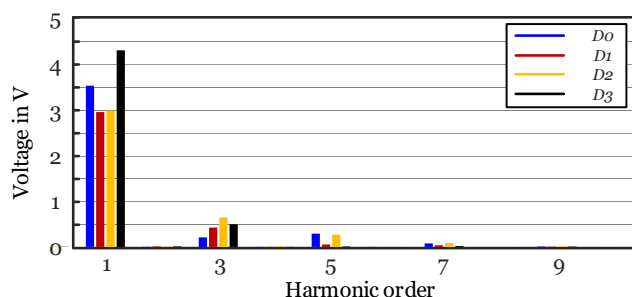
#### APPENDIX D

##### HARMONIC ANALYSIS OF THE BACK-EMF WAVEFORMS

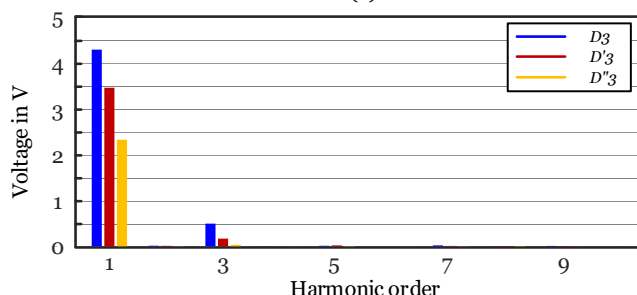
Fig. 22 shows the harmonic content of the back-EMF waveform of different investigated designs in Figs. 5, 13(b), and 16(c).

#### REFERENCES

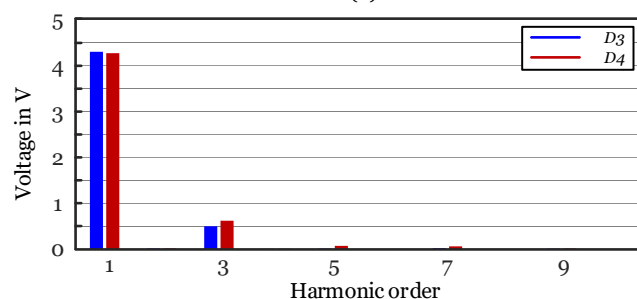
- [1] N. Saed, S. Asgari and A. Muetze, "On the Effect of Claw Geometry on the Vibration of Single-Phase Claw-Pole BLDC Machines," *2023 11th International Conference on Power Electronics and ECCE Asia (ICPE 2023 - ECCE Asia)*, Jeju Island, Korea, Republic of, 2023, pp. 142-147.
- [2] W. H. Yeadon and A. W. Yeadon, *Handbook of Small Electric Motors*, McGraw-Hill, New York, NY, USA, 2001.
- [3] S. Leitner, H. Gruebler and A. Muetze, "Cogging Torque Minimization and Performance of the Sub-Fractional HP BLDC Claw-Pole Motor," *IEEE Transactions on Industry Applications*, vol. 55, no. 5, pp. 4653-4664, Sept.-Oct. 2019.
- [4] S. Leitner, H. Gruebler and A. Muetze, "Innovative Low-Cost Sub-Fractional HP BLDC Claw-Pole Machine Design for Fan Applications," *IEEE Transactions on Industry Applications*, vol. 55, no. 3, pp. 2558-2568, May-June 2019.
- [5] N. Saed, S. Leitner, F. Krall, and A. Muetze, "Noise and vibration characteristics of sub-fractional horsepower single-phase BLDC drives," *Elektrotech. Inftech.*, vol. 139, pp. 260-270, 2022.
- [6] K. Yamazaki, R. Suzuki, M. Nuka and M. Masegi, "Characteristics improvement of claw-pole alternators by reducing armature reaction," in *2017 IEEE International Electric Machines and Drives Conference (IEMDC)*, Miami, FL, USA, 2017, pp. 1-6.
- [7] S. Wu, S. Zuo and Y. Zhang, "Optimization for Electromagnetic Noise Reduction in Claw Pole Alternator by Rotor Claw Chamfering," *IEEE Transactions on Industrial Electronics*, vol. 65, no. 12, pp. 9325-9335, Dec. 2018.
- [8] J.-H. Lee and S.-Y. Jung, "Noise Reduction Design with Trapezoidal Back-EMF and Asymmetric Air-Gap for Single-Phase BLDC Refrigerator Cooling Fan Motor," *Energies*, vol. 14, no. 17, article 5467, 2021.



(a)



(b)



(c)

Fig. 22. Harmonic analysis of the back-EMF waveform of the investigated designs.

- [9] M. S. Islam, S. Mir and T. Sebastian, "Issues in reducing the cogging torque of mass-produced permanent-magnet brushless DC motor," in *IEEE Transactions on Industry Applications*, vol. 40, no. 3, pp. 813-820, May-June 2004.
- [10] R. Krishnan, *Permanent Magnet Synchronous and Brushless DC Motor Drives*, CRC Press, Boca Raton, FL, USA, 2010.
- [11] JSOL Corporation, "Simulation Technology for Electromagnetical Design," <http://www.jmag-international.com/>, accessed on 10-03-2023.
- [12] N. Bianchi and S. Bolognani, "Design techniques for reducing the cogging torque in surface-mounted PM motors," in *IEEE Transactions on Industry Applications*, vol. 38, no. 5, pp. 1259-1265, Sept.-Oct. 2002.
- [13] N. Saed, S. Leitner and A. Muetze, "Noise and Vibration Characteristics of the Single-Phase Claw-Pole BLDC Machine with Different Stator Topologies," in *IKMT 2022; 13. GMM/ETG-Symposium*, Linz, Austria, 2022, pp. 1-5.
- [14] S. Leitner, N. Saed and A. Muetze, "Analysis of Claw Deflections and Radial Magnetic Forces in Low-Cost Sub-Fractional Horsepower BLDC Claw-Pole Motors," *2021 IEEE Energy Conversion Congress and Exposition (ECCE)*, 2021, pp. 3909-3914.
- [15] A. P. Boreasi and R. J. Schmidt, *Advanced Mechanics of Materials*. John Wiley & Sons, 2002.
- [16] H. Gruebler, S. Leitner, A. Muetze and G. Schoener, "Improved Switching Strategy for a Single-Phase Brushless Direct Current Fan Drive and its Impact on Efficiency," in *IEEE Transactions on Industry Applications*, vol. 54, no. 6, pp. 6050-6059, Nov.-Dec. 2018.
- [17] N. Saed, S. Asgari and A. Muetze, "Vibration Analysis of Single-Phase Brushless DC Fan Drives Considering Position Signal Error," in *IEEE Transactions on Industry Applications*, vol. 60, no. 4, pp. 6242-6251, July-Aug. 2024.

- [18] Bielert, F. (2014): Zusatzaggregate – Akustische Anforderungen, Volkswagen Konzernnorm. VW 82 469.
- [19] Byung-Il Kwon, Byoung-Yull Yang, Seung-Chan Park and Young-Sun Jin, "Novel topology of unequal air gap in a single-phase brushless DC motor," in IEEE Transactions on Magnetics, vol. 37, no. 5, pp. 3723-3726, Sept. 2001.
- [20] Y. -U. Park, J. -H. Cho and D. -k. Kim, "Cogging Torque Reduction of Single-Phase Brushless DC Motor With a Tapered Air-Gap Using Optimizing Notch Size and Position," in IEEE Transactions on Industry Applications, vol. 51, no. 6, pp. 4455-4463, Nov.-Dec. 2015.
- [21] C. -L. Chiu, Y. -T. Chen and W. -S. Jhang, "Properties of Cogging Torque, Starting Torque, and Electrical Circuits for the Single-Phase Brushless DC Motor," in IEEE Transactions on Magnetics, vol. 44, no. 10, pp. 2317-2323, Oct. 2008.
- [22] PCB Piezotronics. (2022) Triaxial force sensor 260M36. Accessed on May 9th, 2024. [Online]. Available: [https://www.pcbpiezotronics.de/produkte/datenblatt/?untergruppe=kra\\_tri\\_ax&h=PCB&m=260M36](https://www.pcbpiezotronics.de/produkte/datenblatt/?untergruppe=kra_tri_ax&h=PCB&m=260M36).
- [23] National Instruments, (2023) cDAQ-9174. Accessed on May 9th, 2024. [Online]. Available: <https://www.ni.com/de-at/shop/model/cdaq-9174.html>
- [24] National Instruments, (2023) NI-9232. Accessed on May 9th, 2024. [Online]. Available: <https://www.ni.com/de-at/shop/model/ni-9232.html>.